Nano Research

Open Access

Research Article

Mechanically robust carbon nanotube composite fibers via reinforced intertube interactions

Yunhang Li[1,2,3,§], Jiankun Huang[4,§], Xudong Lei[5,6], Tongzhao Sun[3], Xianqian Wu[5,6], Yuanlong Shao[3,4], Jin Zhang[3,4], Yongyi Zhang[1,2] ✉, and Muqiang Jian[3,4] ✉

[1] *School of Nano-Tech and Nano-Bionics, University of Science and Technology of China, Hefei 230026, China*
[2] *Key Laboratory of Multifunctional Nanomaterials and Smart Systems, Suzhou Institute of Nano-Tech and Nano-Bionics, Chinese Academy of Sciences, Suzhou 215123, China*
[3] *Beijing Graphene Institute (BGI), Beijing 100095, China*
[4] *School of Materials Science and Engineering, Beijing National Laboratory for Molecular Sciences, College of Chemistry and Molecular Engineering, Peking University, Beijing 100871, China*
[5] *Key Laboratory of Mechanics in Fluid Solid Coupling Systems, Institute of Mechanics, Chinese Academy of Sciences, Beijing 100190, China*
[6] *School of Engineering Science, University of Chinese Academy of Sciences, Beijing 100049, China*
§ *Yunhang Li and Jiankun Huang contributed equally to this work.*

Cite this article: *Nano Research*, **2026**, *19*, 94908598. https://doi.org/10.26599/NR.2026.94908598

ABSTRACT: Carbon nanotube fibers (CNTFs) offer exceptional intrinsic properties but are often limited by assembly defects and inefficient intertube load transfer. Here, we report a wet-spinning strategy enabled by poly(p-phenylene-2,6-benzobisoxazole) nanofibers and chains (PBOs)-reinforced intertube interactions to fabricate mechanically robust PBO/carbon nanotube (CNT) composite fibers (PCNTFs). By optimizing the PBOs content, highly aligned and densely packed CNT networks are formed and stabilized by a hydrogen-bonding interfacial architecture. Comprehensive structural characterization reveals maximized nanotube orientation, minimized void volume, and strengthened interfacial interactions at the optimal composition. As a result, the PCNTFs achieve a high tensile strength of 3.52 GPa, a Young's modulus of 306 GPa, and a toughness of 71.5 MJ/m^3, representing a 2.7-fold enhancement in toughness compared with pristine CNTFs. *In situ* Raman spectroscopy, stress–relaxation analysis, and fracture morphology observations further confirm the critical role of hydrogen-bonding-mediated interfacial interactions in governing efficient stress transfer and energy dissipation. Moreover, the optimized fibers exhibit a high specific penetration energy of 1.39 MJ/kg under high-speed impact, exceeding that of conventional impact-resistant fibers. This work establishes a scalable interfacial design strategy for CNT-based fibers with simultaneously high strength and toughness and provides a feasible pathway toward next-generation fibers for structural and multifunctional applications.

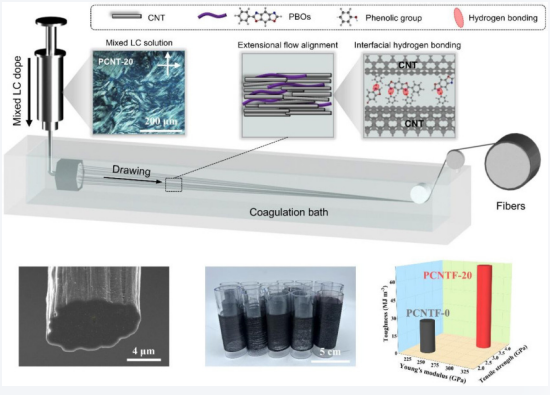

KEYWORDS: carbon nanotube fiber, wet spinning, interfacial interactions, hydrogen-bonding, poly(p-phenylene-2,6-benzobisoxazole)

1 Introduction

Carbon nanotubes (CNTs) possess extraordinary intrinsic mechanical, electrical, and thermal properties [1–3], making them highly attractive building blocks for next-generation high-performance fibers [4–10]. However, translating these exceptional nanoscale properties into macroscopic CNT fibers (CNTFs) remains a long-standing challenge. In practical CNTFs, the mechanical performance is often limited by hierarchical assembly defects, insufficient nanotube alignment, and weak intertube interactions, which promote premature nanotube slippage under external loading [11, 12]. These multiscale structural imperfections severely restrict effective stress transfer across the fiber hierarchy, resulting in mechanical properties far below the theoretical

Received: January 4, 2026; **Revised:** February 12, 2026
Accepted: February 24, 2026

✉Address correspondence to Muqiang Jian, jianmq-cnc@pku.edu.cn; Yongyi Zhang, yyzhang2011@sinano.ac.cn

potential of CNT assemblies. To address these challenges, considerable efforts have been devoted to improving CNTF performance through the control of CNT quality, such as aspect ratio and purity [13–17], optimization of spinning processes [18–21], and application of post-treatment strategies such as wet-stretching [22–25], mechanical densification [26–28], and high-temperature annealing [29–31]. Among various fabrication routes, wet spinning from chlorosulfonic acid (CSA)-based liquid-crystalline dopes has emerged as a particularly powerful and scalable method, enabling the formation of highly aligned CNTFs with relatively high structural uniformity [32]. However, even in optimized wet-spun CNTFs, inter- and intra-bundle voids are inevitably generated during coagulation and solvent exchange, while the van der Waals-dominated intertube interfaces remain too weak to support efficient load transfer under deformation.

To overcome these limitations, reinforcing intertube interactions has become a central design principle for high-performance CNTFs. Various strategies have been explored, including microwave-induced welding [33], hybridization with graphene or polymeric binders [34–36], and high-temperature annealing [29, 37, 38]. For example, microwave-induced welding of polymer-infiltrated CNTFs has been shown to significantly enhance both static and dynamic tensile strength by reinforcing intertube cohesion [33], although this approach often involves increased processing complexity and limited scalability. Alternatively, hybridization with two-dimensional graphene oxide or polymers can effectively reduce voids, improve alignment, and enhance interfacial intereactions, leading to simultaneous improvements in tensile strength, modulus, and toughness [34, 35]. These advances suggest that polymer-mediated interfacial regulation represents a promising and versatile approach to overcoming the structural limitations of CNTFs. In particular, rigid-rod aromatic polymers capable of forming strong and reversible noncovalent interactions with CNTs offer unique advantages for reinforcing intertube interactions without sacrificing structural alignment. Poly(p-phenylene-2,6-benzobisoxazole) (PBO), often referred to as the "super fiber of the 21st century", is well known for its exceptional tensile strength, high Yong's modulus, and excellent temperature resistance [39, 40]. These properties originate from its rigid, rod-like, and highly oriented molecular chains, which consists of alternating arrangement of benzene rings and oxazole rings [41]. Such characteristics make PBO an attractive candidate for interfacial reinforcement in CNT-based composite fibers. However, a systematic understanding of how polymer-reinforced intertube interactions regulate multiscale structure, void evolution, and energy dissipation in CNT composite fibers remains incomplete.

In this study, we report a PBO nanofibers and chains (PBOs)-reinforced intertube interaction strategy to fabricate mechanically robust PBOs/functionalized CNTs (FCNTs) composite fibers (PCNTFs). Upon integration with FCNTs, the oxygen and nitrogen atoms within PBOs can form hydrogen bonding networks with the hydroxyl groups on FCNTs, thereby reinforcing intertube interactions and generating a tightly coupled interfacial architecture. Comprehensive multiscale structural and mechanical analyses reveal that an optimal PBOs content simultaneously maximizes nanotube orientation, minimizes void volume, and strengthens interfacial interactions, resulting in the PCNTFs with a high tensile strength of 3.52 GPa and a toughness of 71.5 MJ/m^3. Importantly, the optimized fibers also exhibit a high specific penetration energy under high-speed impact. This work provides a scalable interfacial design strategy for high-performance CNT-based fibers and opens new opportunities for advanced structural and multifunctional applications.

2 Experimental

2.1 Materials

Raw CNTs were supplied by Cnano (Jiangsu Cnano Technology Co., Ltd.). Chlorosulfonic acid (CSA, 97.0%) and acetone (> 99.5%) were purchased from Sinopharm Chemical Reagent Co., Ltd. Sodium nitrite ($NaNO_2$, > 99.99%) and p-aminophenol (C_6H_7NO, ≥ 98%) were obtained from Macklin Reagent Co., Ltd. PBO fibers were provided by China Bluestar Chengrand Research Institute of Chemical Industry Co., Ltd.

2.2 Preparation of FCNTs

Raw CNTs were purified prior to use. The as-received CNTs were first annealed in air at 400 °C for 6 h, and then dispersed in 12 M HCl for 12 h to eliminate remaining metal catalysts. The resulting suspension was subjected to vacuum filtration and thoroughly washed with deionized water until neutral. The purified CNTs were then frozen and dried via freeze-drying overnight. The dried CNTs were dispersing in CSA at a concentration of 10 mg/mL using a speed mixer. The equimolar amounts of C_6H_7NO and $NaNO_2$ were then added to the solution at a 1:60 molar ratio relative to the carbon content of CNTs. The resulting mixture was subsequently added dropwise into deionized water under continuous stirring. **Safety note**: This reaction was highly exothermic and releases significant acidic fumes; therefore, all procedures must be performed in a chemical fume hood. Appropriate personal protective equipment, including goggles, face shields or masks, lab coats, and acid-resistant gloves, was required. The FCNTs rapidly precipitated from the solution. The precipitate was collected by vacuum filtration, extensively washed with deionized water, and freeze-dried for 48 h.

2.3 Preparation of PCNTFs

PBO fibers were vigorously washed with acetone several times, and then dried at 60 °C for 12 h. Liquid crystal spinning dopes were prepared by dispersing FCNTs and PBO fibers into CSA solutions at various mass ratios, followed by continuous stirring at room temperature. Wet-spun composite fibers were prepared by extruding the dopes into an acetone coagulation bath through a spinneret with inner diameter of 100 μm. The dope extrusion rates were controlled at between 0.05 and 0.3 mL/min using a syringe pump. A draw ratio of 2.0 was applied by adjusting the relative extrusion and winding rates. The resulting PCNTFs were then washed with deionized water and finally dried at 70 °C for 24 h.

3 Results and discussion

3.1 Preparation and microstructures of PCNTFs

We first achieved the covalent functionalization of purified CNTs via aryl diazonium chemistry [42–44]. The few-walled CNTs, with an average diameter of about 2.5 nm and an average aspect ratio of approximately 4400 (Fig. S1 in the Electronic Supplementary Material (ESM)) [45, 46], were dispersed in CSA, followed by the addition of sodium nitrite and p-aminophenol. The acidic mixture

containing CNTs and *in situ*-generated diazonium species was then added the drop-by-drop to deionized water, enabling the introduction of phenolic groups and paired hydroxyl functionalities on the CNT sidewalls [44]. Raman spectroscopy provides clear evidence of successful functionalization. The intensity ratio of the G band to the D band (I_G/I_D) decreases markedly from 51.3 ± 9.7 for purified CNTs to 27.8 ± 4.1 for FCNTs (Fig. S2 in the ESM), signaling the introduction of covalent defects associated with surface functional groups [47]. X-ray photoelectron spectroscopy (XPS) further confirms this chemical modification, as evidenced by an increase in oxygen content from 1.84 at.% to 4.46 at.%, together with a pronounced enhancement of the C–O component in the C 1s spectrum (Fig. S3 in the ESM). Thermogravimetric analysis (TGA) also verifies the presence of functional groups (Fig. S4 in the ESM). While purified CNTs exhibit negligible mass loss due to their high purity and crystallinity, FCNTs show an initial mass loss of approximately 10 wt.% around 250 °C, followed by a secondary mass loss near 550 °C. This two-step mass loss behavior is consistent with the characteristic feature of diazonium-derived functionalization, in which paired functional groups are simultaneously grafted onto the CNT surface [44, 48].

As illustrated in Fig. 1(a), we further developed a PBOs-reinforced intertube interaction strategy integrated into a wet spinning process to produce mechanically robust PCNTFs. PBOs/FCNT spinning dopes were prepared by adding 5 wt.%, 10 wt.%, 20 wt.%, and 30 wt.% PBOs (designated PCNT-5, PCNT-10, PCNT-20, and PCNT-30, respectively) into CNT/CSA liquid-crystalline solutions. Polarized optical microscopy reveals that all PBOs/FCNT spinning dopes exhibit well-defined nematic liquid-crystalline textures, even at a PBOs content as high as 30 wt.% (Fig. 1(b) and Fig. S5 in the ESM). Maintaining a nematic liquid-crystalline phase is critical for promoting CNT alignment and dense packing during fiber formation, which are key structural prerequisites for high mechanical performance [18, 19, 35, 49]. The liquid-crystalline spinning dopes, including FCNT, PCNT-5, PCNT-10, PCNT-20, and PCNT-30, were extruded into the coagulation bath through a spinneret (Fig. 1(c)), and subsequently drawn at a draw ratio of 2.0. This process induces synergistic shear-flow- and extensional-flow-induced alignment of CNTs and polymers during coagulation and solidification. After washing and drying, the as-spun fibers were continuously collected onto rollers, yielding PCNTF-0, PCNTF-5, PCNTF-10, PCNTF-20, and PCNTF-30, respectively. The resulting composite fibers exhibit a highly aligned and densely packed internal microstructure, further reinforced by an extensive hydrogen-bonding network formed between FCNTs and PBOs. This hierarchical structural organization substantially reinforces interfacial interactions and load transfer efficiency, thereby enabling the improved mechanical performance of the PCNTFs. Moreover, the continuous winding of mechanically robust fibers onto collection rollers highlights the scalability and large-area production potential of this wet-spinning strategy (Fig. 1(d)).

The PBOs content plays an important role in governing microstructure of the fibers, providing a critical link between interfacial design and the multiscale structural features. We first systematically compared the surface and cross-sectional morphologies of the as-spun fibers. Surface scanning electron microscopy (SEM) images show that PCNTF-20 exhibits a uniform and smooth exterior with minimal surface grooves, and the higher-magnification images confirm the well-aligned orientation of nanotubes along the fiber axis (Figs. 2(a) and 2(b)). In contrast, pristine CNTF and PCNTF-0 display a higher density of surface grooves and a comparatively rougher morphology (Fig. S6 in the ESM). Cross-sectional SEM images further reveal that PCNTF-20

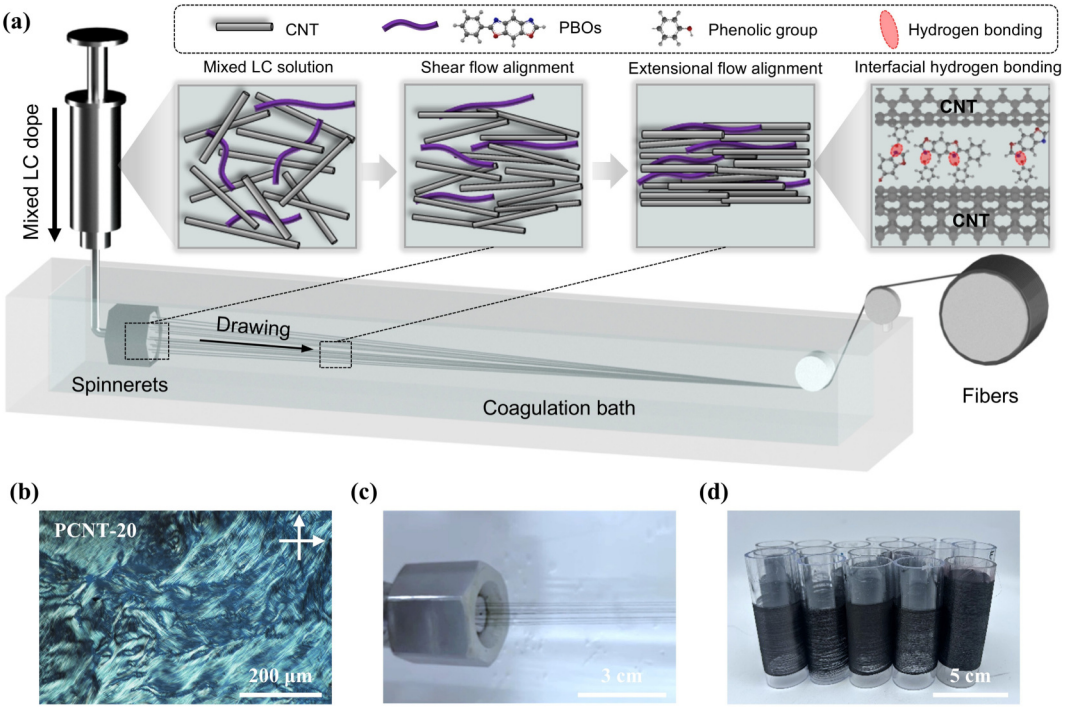

Figure 1 Wet-spinning-enabled structural organization and mechanical reinforcement of FCNTFs. (a) Schematic illustration of the wet-spinning process, in which liquid-crystalline alignment and coagulation-induced densification generate highly oriented PCNTFs reinforced by an interfacial hydrogen-bonding network, resulting in enhanced mechanical robustness. (b) Polarized optical image of the homogeneously mixed PBOs/FCNT liquid-crystalline spinning dope. (c) Photograph of continuous nascent fiber formation during extrusion through a 10-hole spinneret. (d) Digital image of the as-spun PCNTFs.

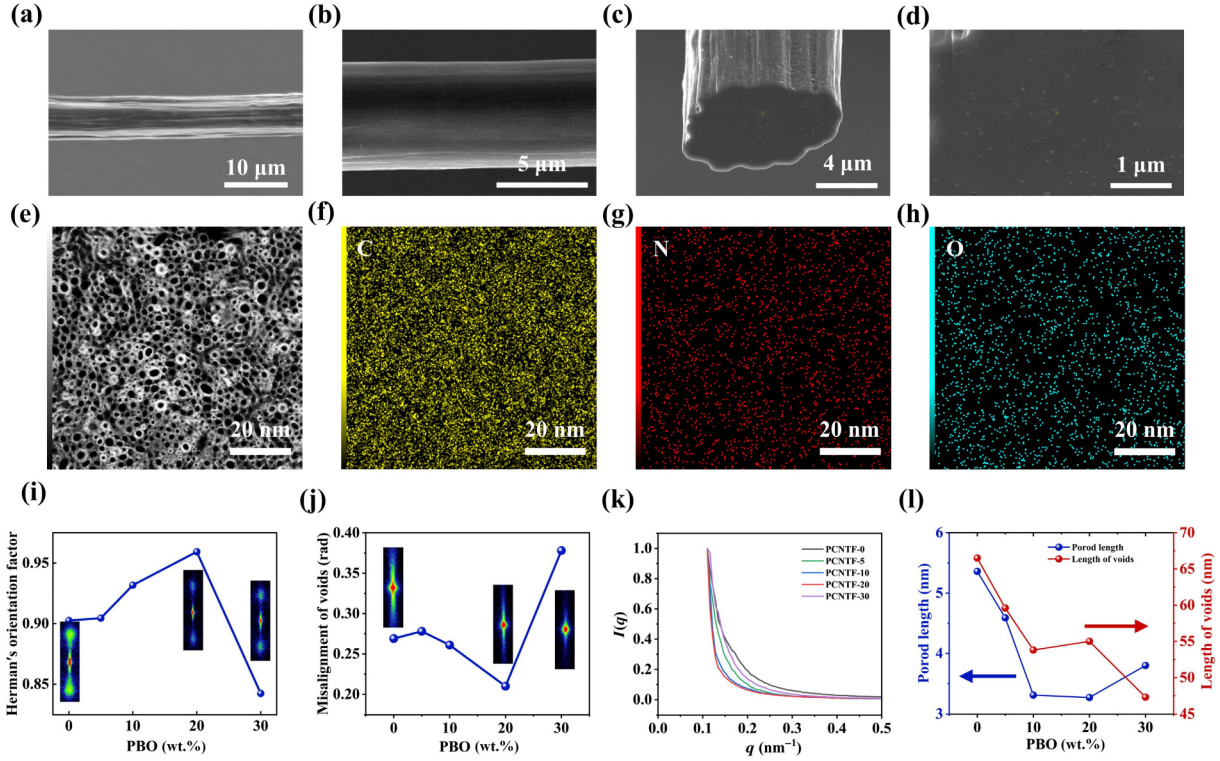

Figure 2 Multiscale structural characterization of PCNTFs. ((a)–(d)) SEM images of ((a) and (b)) the surface morphology and ((c) and (d)) cross-section structure of PCNTF-20. (e) HAADF-STEM image and ((f)–(h)) corresponding EDS elemental mappings of (f) C, (g) N, and (h) O for PCNTF-20. (i) WAXS patterns and corresponding Herman's orientation factors of the fibers. (j) Misalignment angles of voids along the fiber axis. (k) Scattering intensity as a function of scattering vector along the equatorial direction of SAXS patterns for PCNTFs. (l) Characteristic length and Porod length of voids derived from SAXS analysis.

achieves a markedly higher packing density and a reduced void volume compared with the other samples (Figs. 2(c) and 2(d), and Figs. S7 and S8 in the ESM). Consistently, high-angle annular dark-field scanning transmission electron microscopy (HAADF-STEM) images provide direct evidence of compact nanotube packing within PCNTF-20 (Fig. 2(e) and Fig. S9 in the ESM). These structural observations collectively indicate that, at a PBOs content of 20 wt.%, enhanced FCNT alignment and densification are achieved [35]. To further examine the spatial distribution of PBOs within PCNTF-20, energy dispersive X-ray spectroscopy (EDS) mapping was conducted. The homogeneous distribution of carbon (C), oxygen (O), and nitrogen (N) across the fiber cross-section confirms that PBOs are uniformly incorporated among FCNTs during fiber formation (Figs. 2(f)–2(h)), suggesting the well-developed interfacial contact within the composite structure. This compositional uniformity also implies favorable compatibility between PBOs and FCNTs in the CSA system, enabling their co-dispersion and synergistic alignment during wet spinning process, which facilitates the formation of densely packed and mechanically robust composite fibers.

The resulting fiber microstructures were further systematically characterized by wide-angle X-ray scattering (WAXS) and small-angle X-ray scattering (SAXS), which together reveal the critical role of PBOs content in fiber formation. As the PBOs content increases from 0 wt.% to 20 wt.%, the spindle-shaped diffraction peak located at $2\theta \approx 26°$ in WAXS patterns progressively narrows, whereas a pronounced peak broadening emerges at PCNTF-30 (Fig. 2(i) and Fig. S10(a) in the ESM). This evolution reflects a PBOs-content-dependent transition in FCNT alignment. Correspondingly, PCNTF-20 exhibits the highest Herman's orientation factor of 0.96, surpassing those of the other samples, while a further increase in the PBOs content to 30 wt.% results in a reduced orientation factor of 0.84. These results demonstrate that an appropriate amount of PBOs facilitates the axial alignment of FCNTs within the fibers, whereas excessive PBOs introduce structural misalignment and lead to structural disorder, likely arising from polymer aggregation [23, 35]. The molecular orientation trends revealed by WAXS are in strong agreement with void alignment characteristics derived from SAXS analysis (Fig. 2(j)). Specifically, PCNTF-20 displays the sharpest equatorial streak, indicative of highly oriented voids distribution along the fiber axis, whereas the equatorial scattering of PCNTF-30 evolves into rounded elliptical features, reflecting increased void misalignment [29]. The consistency between WAXS-derived Herman's orientation factors and SAXS-derived void misalignment angles demonstrates coherent structural evolution across multiple length scales [27, 29, 50–52]. Moreover, the analysis of the one-dimensional SAXS intensity profile as a function of the scattering vector reveals that the void volume fraction reaches a minimum at a PBOs content of 20 wt.% (Fig. 2(k)). These results demonstrate that optimizing the PBOs content enables the simultaneous enhancement of nanotube alignment and structural densification within PCNTFs, which is essential for achieving high mechanical performance.

Ruland's method and Porod's law were further employed to quantify the void length and Porod length (void thickness) of PCNTFs (Fig. 2(l) and Fig. S10(b) in the ESM) [29, 53, 54]. With increasing PBOs content, the void length decreases from PCNTF-0 to PCNTF-30, shrinking from 66.5 to 47.3 nm. Similarly, the void thickness decreases from 5.4 nm in PCNTF-0 to 3.3 nm in PCNTF-20, but rises to 3.8 nm in PCNTF-30. Considering

both parameters, the void volume continuously decreases from PCNTF-0 to PCNTF-20, indicating improved structural compaction. In contrast, PCNTF-30 shows a marked increase in void volume, with the thickening of voids indicating reduced void orientation and structural order [53, 54]. These observations confirm that the optimization of PBOs content promotes both orientation and densification of the void structure within PCNTFs. According to Porod's law, the interfacial factor (σ) can be obtained from the slope (k) of the $\ln[I(q)q^4]$ versus q^2 plots using the relation $\sigma = \sqrt{|k|}$ [50–52]. This factor represents the thickness of the interfacial transition region within a two-phase system and thus provides a structural descriptor of changes in the interfacial stress-transfer region between PBOs and FCNTs in the PCNTFs. Consistent with PBOs-induced interfacial evolution in PCNTFs, the σ value increases from 1.7 nm for PCNTF-5 to 2.3 nm for PCNTF-20 (Figs. S10(c) and S11 in the ESM), indicating reinforced interfacial contact and tighter stacking between PBOs and FCNTs, which leads to the high mechanical performance of PCNTF-20. In contrast, the σ value decreases markedly to 1.9 nm for PCNTF-30, suggesting the onset of polymer aggregation and interfacial disruption within the fiber structure [50–52, 55, 56].

3.2 Performance of PCNTFs

Regulating the PBOs content in the spinning dope enables systematic optimization of both the mechanical and electrical performance of the composite fibers, with PCNTF-20 exhibiting the most favorable properties. Tensile testing reveals that PCNTF-20 exhibits the highest tensile strength, Young's modulus, and toughness among all samples. Specifically, the tensile strength increases from 2.20 ± 0.35 GPa for PCNTF-0 to 3.52 ± 0.08 GPa for PCNTF-20, corresponding to an improvement of approximately 60%, whereas the Young's modulus increases from 240 ± 44 to 306 ± 26 GPa (Figs. 3(a)–3(c) and Table S1 in the ESM). Furthermore, the toughness of PCNTF-20 (71.5 ± 7.6 MJ/m³) is 2.7 times that of PCNTF-0 (26.6 ± 7.0 MJ/m³) (Fig. 3(d)). Additionally, pristine CNTFs exhibit a tensile strength of 1.92 ± 0.26 GPa, which is lower than that of PCNTF-20 (Table S1 in the ESM). This difference suggests that covalent functionalization of CNTs promotes the initial formation of hydrogen-bonded interfacial networks between functional groups, thereby enhancing intertube interactions and improving tensile strength of the fibers. We further performed a direct literature comparison of mechanical performance for CNTFs produced from CNTs with different aspect ratios (Fig. S12 in the ESM). Fibers derived from lower-aspect-ratio CNTs tend to exhibit reduced tensile strength and modulus compared with those produced from high-aspect-ratio CNTs, revealing the central role of aspect ratio in governing fiber performance. Notably, both the tensile strength and Young's modulus of our PCNTFs fall within the performance envelope defined by the fitted aspect-ratio-dependent trendline, indicating that their mechanical properties are consistent with structural expectations. In addition to mechanical reinforcement, the incorporation of PBO also enhances the electrical conductivity of the composite fibers. The electrical conductivity of PCNTFs increases from 1.62 ± 0.25 MS/m for PCNTF-0 to 3.65 ± 0.40 MS/m for PCNTF-20 (Table S2 in the ESM). This enhancement, despite the intrinsically insulating nature of PBOs, can be attributed to improved fiber densification and nanotube alignment, which facilitate the formation of continuous and well-connected conductive pathways within the FCNT networks [27, 28, 35, 57]. In contrast, PCNTF-30 exhibits markedly reduced mechanical and electrical performance compared with PCNTF-20. Based on the aforementioned multiscale structural analyses obtained from WAXS and SAXS, it can be inferred that excessive

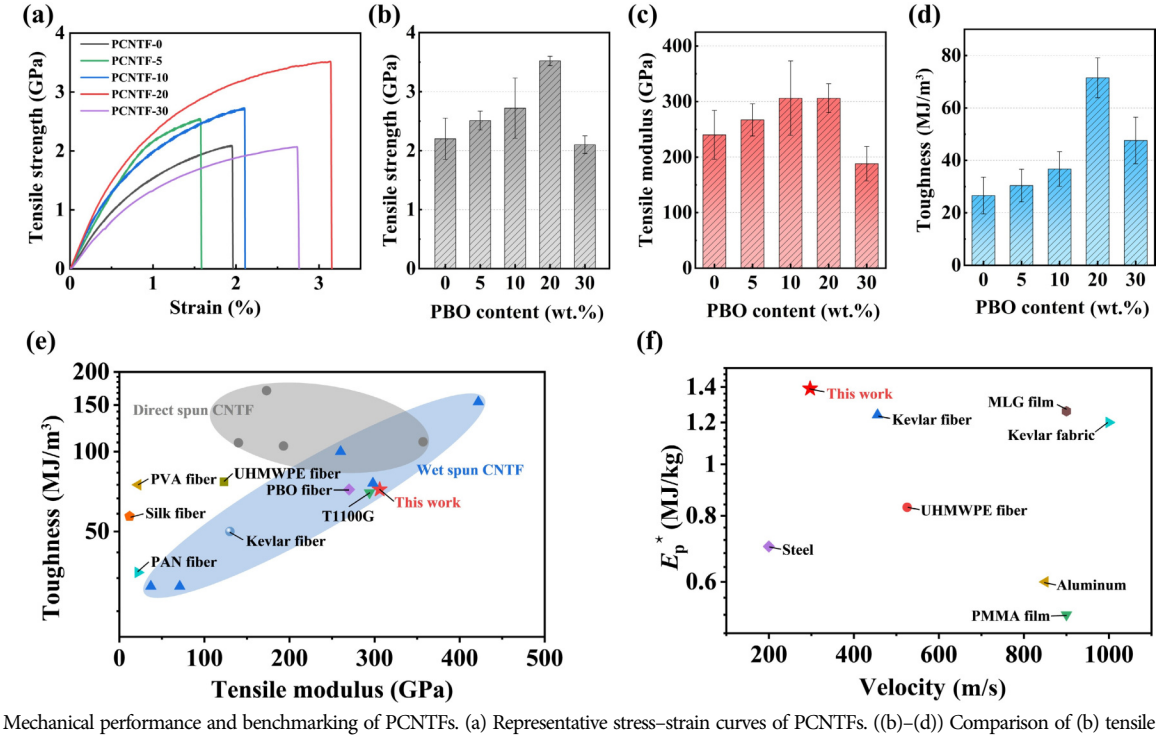

Figure 3 Mechanical performance and benchmarking of PCNTFs. (a) Representative stress–strain curves of PCNTFs. ((b)–(d)) Comparison of (b) tensile strength, (c) Young's modulus, and (d) toughness of PCNTFs with different PBOs contents. (e) Comparison of toughness and Young's modulus of PCNTF-20 with those of other representative high-performance fibers. Here, PVA, UHMWPE, and PAN represent polyvinyl alcohol, ultra-high molecular weight polyethylene, and polyacrylonitrile, respectively. (f) Comparison of specific penetration energy between PCNTF-20 and typical impact-resistant materials.

PBOs introduction promotes molecular aggregation, which disrupts the aligned FCNT network within the fibers. Meanwhile, the void units become larger and more disordered, accompanied by an increase in the overall void volume fraction. These structural degradations weaken the load-transfer efficiency and compromise the continuity of conductive pathways, ultimately resulting in the pronounced deterioration of the mechanical and electrical properties of PCNTF-30. Compared with typical high-performance fibers, PCNTF-20 exhibits a Young's modulus and a toughness that are comparable to, or exceed, those of conventional high-performance organic fibers, polyacrylonitrile-based carbon fibers, and previously reported CNTFs (Fig. 3(e) and Table S3 in the ESM).

We further employed laser-induced micro-projectile impact testing to evaluate the high-velocity impact energy absorption capability of the fibers. In this technique, a micro-projectile is rapidly accelerated by a laser and launched toward the PCNTFs (Fig. S13 in the ESM), inducing characteristic dynamic responses under extremely high strain rates. The specific penetration energy, defined as the impact energy absorbed per unit mass of the fiber, is calculated from the kinetic energy difference between the incident and residual velocities of the projectile, both of which are captured frame-by-frame using a high-speed camera. It should be noted that specific penetration energy is fundamentally different from the specific energy dissipation power [27, 33, 58], which characterizes the rate of energy dissipation during non-penetrating deformation and is intrinsically a power-based metric. In contrast, as a key indicator of impact resistant performance, the specific penetration energy directly reflects the ability of a material to dissipate energy during high-strain-rate penetration events [28, 59]. PCNTFs exhibit excellent impact energy absorption performance, with the specific penetration energy values increasing from ~ 0.96 MJ/kg for PCNTF-0 to ~ 1.39 MJ/kg for PCNTF-20 (Fig. 3(f) and Table S4 in the ESM), corresponding to an improvement of about 45%. Notably, this value exceeds that of widely used impact-resistant fibers such as Kevlar fibers (~ 1.24 MJ/kg) and is comparable to CNTFs reported using plant cell wall-inspired interfacial bridging strategies and CNTs-reinforced heterocyclic aramid fiber systems [28, 59]. However, it remains lower than values reported for ultrathin CNT films and ion-irradiated assemblies [60, 61]. This difference arises from intrinsic distinctions in size scale, structural architecture, and deformation mechanisms between CNTFs and CNT films, which govern their respective energy dissipation pathways [27, 28, 58]. The outstanding energy absorption capability of PCNTF-20 is attributed to the intrinsic impact resistance of CNTs combined with multilevel energy dissipation enabled by the dynamic and reversible reconstruction of hydrogen-bonding interfaces during high-rate deformation [62].

3.3 Strengthening mechanisms

To understand the strengthening mechanism, we conducted *in situ* Raman spectroscopy, stress–relaxation experiments, and Fourier transform infrared spectroscopy (FTIR). *In situ* Raman spectroscopy was used to investigate the load-transfer efficiency, where the strain-induced shift of G′-band serves as a quantitative indicator of stress transfer within the nanotube network [27, 63]. PCNTF-0 shows a modest G′-band shift of −16.8 cm^{-1} under the applied strain (Fig. 4(a)), consistent with its inefficient stress transfer and inferior mechanical performance. In contrast, PCNTF-20 exhibits a more pronounced downshift of −19.5 cm^{-1} (Fig. 4(b)), which is significantly higher than those of the other fibers (Fig. 4(c) and Fig. S14 in the ESM), indicating strong interfacial cohesion and more efficient load distribution throughout the network. Stress–relaxation tests were further performed to evaluate the stress retention behavior of PCNTFs under a constant strain of 1%. PCNTF-20 exhibits the highest stress retention (Fig. 4(d)), retaining approximately 92% of its initial stress, which is markedly higher than the 86% retained by PCNTF-0. This enhanced stress retention originates from improved nanotube alignment and strengthened interfacial interactions within PCNTF-20, which effectively

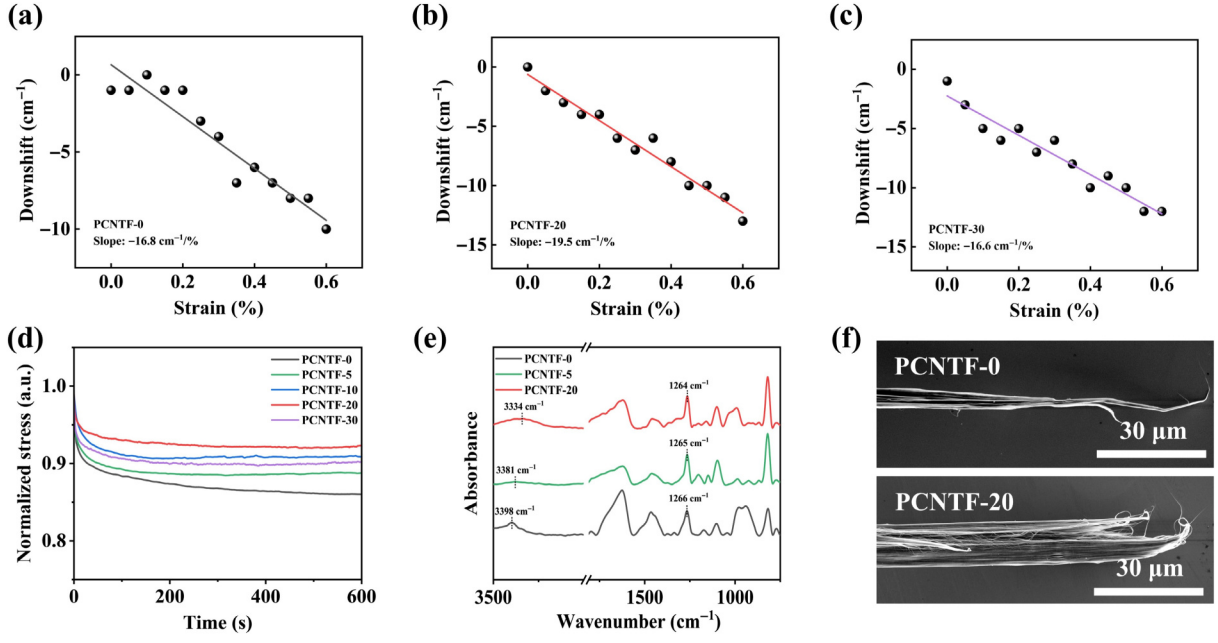

Figure 4 Mechanistic analyses of PCNTFs. ((a)–(c)) Strain-dependence Raman frequency downshifts for (a) PCNTF-0, (b) PCNTF-20, and (c) PCNTF-30 on the applied strains. (d) Stress–relaxation behaviors of different fibers. (e) FTIR spectra for the fibers. (f) SEM images of the fracture morphologies of PCNTF-0 and PCNTF-20.

suppresses nanotube slippage under sustained deformation [27, 28]. FTIR analyses were conducted to elucidate the nature of interfacial interactions within the composite fibers. The stretching vibration of hydroxyl groups, observed at 3398 and 3381 cm^{-1} for PCNTF-0 and PCNTF-5, respectively, exhibits a red shift to 3334 cm^{-1} in PCNTF-20 (Fig. 4(e)), reflecting the progressive strengthening of hydrogen bonding between FCNTs and PBOs [64]. These results confirm the formation of a hydrogen-bonding network at the PBOs–FCNTs interface and demonstrate that the PBOs content effectively regulates the interfacial bonding structure within the fibers. Furthermore, SEM image of fractured fibers reveals that PCNTF-20 exhibits significantly fewer pulled-out nanotube bundles compared with PCNTF-0 (Fig. 4(f)). Such fracture morphologies indicate reinforced interfacial interaction, which limits the pull-out failure and suppresses nanotube slippage during tensile loading. Therefore, these observations demonstrate that PBOs-reinforced intertube interaction strategy synergistically enhances nanotube alignment, structural densification, and interfacial interactions, thereby enabling the simultaneous improvement in tensile strength, Young's modulus, and toughness of the composite fibers.

4 Conclusions

In summary, we demonstrate an effective PBOs-reinforced intertube interaction-enabled wet-spinning strategy for the fabrication of mechanically robust PCNTFs with simultaneously enhanced mechanical and electrical performance. By systematically regulating the PBOs content in the spinning dope, the microstructure and interfacial architecture of the fibers can be tuned. An optimal PBOs content of 20 wt.% enables the formation of highly aligned and densely packed CNT networks reinforced by a hydrogen-bonding interface, resulting in efficient load transfer, suppressed nanotube slippage, and multilevel energy dissipation. Comprehensive multiscale structural analyses reveal that this optimized composition achieves the highest nanotube orientation, minimized void volume, and strengthened interfacial interactions, leading to the superior mechanical performance. Consequently, PCNTF-20 exhibits a combination of high tensile strength, Young's modulus, toughness, and electrical conductivity, and excellent high-velocity impact energy absorption, surpassing or matching the performance of many state-of-the-art high-performance fibers. This work provides clear mechanistic insights into the interfacial regulation of CNT-based composite fibers and offers a scalable design strategy for developing structure-function-integrated fibers for structural and protective applications under extreme loading conditions.

Compared to commercial high-performance fibers such as carbon fibers and PBO fibers, the mechanical performance of current CNTFs remains lower. Future efforts will therefore focus on increasing CNT aspect ratio and dope concentration, optimizing flow-field design and spinning parameters to enhance alignment and densification, and engineering intertube interactions to improve load transfer efficiency. These strategies are expected to collectively advance the structural integrity of CNT assemblies and enable further improvements in the mechanical performance of CNTFs.

Electronic Supplementary Material: Supplementary material (structural characterization of CNTs, XPS spectra of CNTs and FCNTs, SEM images of CNTFs, HAADF-STEM images of PCNTFs, etc.) is available in the online version of this article at https://doi.org/10.26599/NR.2026.94908598.

Data availability

All data needed to support the conclusions in the paper are presented in the manuscript and the Electronic Supplementary Material. Additional data related to this paper may be requested from the corresponding author upon request.

Acknowledgements

This work was supported by the National Key Research and Development Program of China (Nos. 2022YFA1203302 and 2022YFA1203304), the National Natural Science Foundation of China (Nos. 52522202, 52202032, 52021006, and T2188101), the Beijing National Laboratory for Molecular Sciences (Nos. BNLMS202412 and BNLMS-CXTD-202001), the Beijing Natural Science Foundation (No. 2222094), the Strategic Priority Research Program of the Chinese Academy of Sciences (No. XDB36030100), and the Shenzhen Science and Technology Innovation Commission (No. KQTD20221101115627004). We are grateful for technical support for Nano-X from Suzhou Institute of Nano-Tech and Nano-Bionics (SINANO), Chinese Academy of Sciences.

Declaration of competing interest

All the contributing authors report no conflict of interests in this work.

Author contribution statement

The manuscript was written through the contributions of all authors. J. Z., Y. Y. Z., and M. Q. J. conceived the idea and designed the project. Y. H. L. and J. K. H. carried out the preparation of samples and characterization. Y. H. L., J. K. H., X. D. L., T. Z. S., X. Q. W., and Y. L. S. provided the analysis and discussion of experimental results. Y. H. L., J. K. H., M. Q. J., Y. Y. Z., and J. Z. prepared the manuscript. All the authors have approved the final manuscript.

Use of AI statement

None.

References

[1] Bai, Y. X.; Yue, H. J.; Wang, J.; Shen, B. Y.; Sun, S. L.; Wang, S. J.; Wang, H. D.; Li, X. D.; Xu, Z. P.; Zhang, R. F. et al. Super-durable ultralong carbon nanotubes. *Science* **2020**, *369*, 1104–1106.

[2] Jo, S.; Mikhalchan, A.; Hong, S.; Kim, S.; Kim, S. G.; Kim, S. M.; Kim, D. Y.; Ku, B. C.; Vilatela, J. J.; Hwang, J. Y. Highly conductive hybrid carbon nanotube fibers: Strategies and future directions for replacing copper with next-generation conductors. *Compos. Part B: Eng.* **2025**, *300*, 112471.

[3] Zhu, M. Q.; Bai, Y. X.; Gao, R. Y.; Liu, Y. J.; Zhang, P.; Zhang, H.; Liu, L. Q.; Zhang, Z. Failure-analysis of carbon nanotubes and their extreme applications. *Nano Res.* **2023**, *16*, 12364–12383.

[4] Chae, H. G.; Kumar, S. Making strong fibers. *Science* **2008**, *319*, 908–909.

[5] Zhang, X. H.; Lu, W. B.; Zhou, G. H.; Li, Q. W. Understanding the mechanical and conductive properties of carbon nanotube fibers for smart electronics. *Adv. Mater.* **2020**, *32*, 1902028.

[6] Sun, A.; Xu, N.; Wang, Y. F.; Xu, J. Q.; Shi, Z. Z.; Zhang, X. High strength carbon nanotube fibers: Synthesis development, property improvement and possible applications. *New Carbon Mater.* **2025**, *40*, 621–641.

[7] Bulmer, J. S.; Kaniyoor, A.; Elliott, J. A. A meta-analysis of conductive and strong carbon nanotube materials. *Adv. Mater.* **2021**, *33*, 2008432.

[8] Guo, H.; Dong, C. L.; Han, Q. Q.; Jiang, H. Y.; Sun, H. J.; Sun, X. M.; Zhang, S. L.; Peng, H. S. Advancing carbon nanotube fibers: Addressing challenges from production to application. *ACS Cent. Sci.* **2025**, *11*, 855–867.

[9] Wen, Y. Y.; Jian, M. Q.; Huang, J. K.; Luo, J. J.; Qian, L.; Zhang, J. Carbonene fibers: Toward next-generation fiber materials. *Nano Lett.* **2022**, *22*, 6035–6047.

[10] Mikhalchan, A.; Vilatela, J. J. A perspective on high-performance CNT fibres for structural composites. *Carbon* **2019**, *150*, 191–215.

[11] Jung, Y.; Cho, Y. S.; Lee, J. W.; Oh, J. Y.; Park, C. R. How can we make carbon nanotube yarn stronger. *Compos. Sci. Technol.* **2018**, *166*, 95–108.

[12] Wu, K. J.; Zhang, Y. Y.; Yong, Z. Z.; Li, Q. W. Continuous preparation and performance enhancement techniques of carbon nanotube fibers. *Acta Phys. Chim. Sin.* **2022**, *38*, 2106034.

[13] Tsentalovich, D. E.; Headrick, R. J.; Mirri, F.; Hao, J. L.; Behabtu, N.; Young, C. C.; Pasquali, M. Influence of carbon nanotube characteristics on macroscopic fiber properties. *ACS Appl. Mater. Interfaces* **2017**, *9*, 36189–36198.

[14] Taylor, L. W.; Dewey, O. S.; Headrick, R. J.; Komatsu, N.; Peraca, N. M.; Wehmeyer, G.; Kono, J.; Pasquali, M. Improved properties, increased production, and the path to broad adoption of carbon nanotube fibers. *Carbon* **2021**, *171*, 689–694.

[15] Niu, Y. T.; He, Z.; Wang, S.; Zhang, Y. C.; Yang, Z. P.; Zhang, Y. Y.; Yong, Z. Z.; Wu, K. J.; Zhao, L. M.; Guo, Z. H. et al. Continuous carbon nanotube fiber with an extremely high average specific strength of 4.1 $N{\cdot}tex^{-1}$. *Nano Res.* **2025**, *18*, 94907584.

[16] Taylor, L. W.; Dewey, O. S.; Biggers, E. G.; Durán-Chaves, M.; Khoury, J. F.; Pasquali, M. Purification of carbon nanotubes for dissolution in chlorosulfonic acid. *Carbon* **2024**, *228*, 119317.

[17] Cheng, K.; Cheng, L. Z.; Jiang, X. R.; Wang, Z. Y.; Pan, J. Y.; Fang, N.; Zhang, Z. Y.; Qu, S. X.; Lyu, W. B. Effect of CNT oxidation on the processing and properties of superacid-spun cnt fibers. *Chem. Asian J.* **2024**, *19*, e202400327.

[18] Behabtu, N.; Young, C. C.; Tsentalovich, D. E.; Kleinerman, O.; Wang, X.; Ma, A. W. K.; Bengio, E. A.; ter Waarbeek, R. F.; de Jong, J. J.; Hoogerwerf, R. E. et al. Strong, light, multifunctional fibers of carbon nanotubes with ultrahigh conductivity. *Science* **2013**, *339*, 182–186.

[19] Kim, S. G.; Choi, G. M.; Jeong, H. D.; Lee, D.; Kim, S.; Ryu, K. H.; Lee, S.; Kim, J.; Hwang, J. Y.; Kim, N. D. et al. Hierarchical structure control in solution spinning for strong and multifunctional carbon nanotube fibers. *Carbon* **2022**, *196*, 59–69.

[20] Sun, C. Y.; Wang, H. Z.; Gao, Z. Q.; Hou, P. X.; Shi, C.; Liang, Y.; Wang, S. G.; Liu, C.; Cheng, H. M. Ultrathin carbon nanotube fibers with a record high ampacity fabricated using a water coagulation bath. *Adv. Funct. Mater.*, in press, https://doi.org/10.1002/adfm.202518867.

[21] Wang, H. Z.; Jiao, X. Y.; Gao, Z. Q.; Hou, P. X.; Xu, L. L.; Shi, C.; Liang, Y.; Wang, Y. P.; Liu, C. Highly conductive double-wall carbon nanotube fibers produced by dry-jet wet spinning. *Adv. Funct. Mater.* **2024**, *34*, 2404538.

[22] Wu, K. J.; Wang, B.; Niu, Y. T.; Wang, W. J.; Wu, C.; Zhou, T.; Chen, L.; Zhan, X. Z.; Wan, Z. Y.; Wang, S. et al. Carbon nanotube fibers with excellent mechanical and electrical properties by structural realigning and densification. *Nano Res.* **2023**, *16*, 12762–12771.

[23] Li, L. J.; Sun, T. Z.; Lu, S. C.; Chen, Z.; Xu, S. C.; Jian, M. Q.; Zhang, J. Graphene interlocking carbon nanotubes for high-strength and high-conductivity fibers. *ACS Appl. Mater. Interfaces* **2023**, *15*, 5701–5708.

[24] Lee, J.; Lee, D. M.; Jung, Y.; Park, J.; Lee, H. S.; Kim, Y. K.; Park, C. R.; Jeong, H. S.; Kim, S. M. Direct spinning and densification method for high-performance carbon nanotube fibers. *Nat. Commun.* **2019**, *10*, 2962.

[25] Zhang, X.; De Volder, M.; Zhou, W. B.; Issman, L.; Wei, X. J.; Kaniyoor, A.; Terrones Portas, J.; Smail, F.; Wang, Z. B.; Wang, Y. C. et al. Simultaneously enhanced tenacity, rupture work, and thermal conductivity of carbon nanotube fibers by raising effective tube portion. *Sci. Adv.* **2022**, *8*, eabq3515.

[26] Shi, H. L.; Shi, Q. Q.; Zhan, H.; Ai, J. J.; Chen, Y. T.; Wang, J. N. High-strength carbon nanotube fibers from purity control by atomized catalytic pyrolysis and alignment improvement by continuous large prestraining. *Nano Lett.* **2023**, *23*, 10739–10747.

[27] Zhang, X. S.; Lei, X. D.; Jia, X. Z.; Sun, T. Z.; Luo, J. J.; Xu, S. C.; Li, L. J.; Yan, D.; Shao, Y. L.; Yong, Z. Z. et al. Carbon nanotube fibers with dynamic strength up to 14 GPa. *Science* **2024**, *384*, 1318–1323.

[28] Li, X. Y.; Lei, X. D.; Jia, X. Z.; Jian, M. Q.; Sun, T. Z.; Yang, X. Y.; Huang, J. K.; Han, X. C.; Lin, H. L.; Li, Y. H. et al. Plant cell wall-inspired interfacial bridging enables ultrastrong and tough carbon nanotube fibers. *ACS Nano* **2026**, *20*, 593–602.

[29] Lee, D.; Kim, S. G.; Hong, S.; Madrona, C.; Oh, Y.; Park, M.; Komatsu, N.; Taylor, L. W.; Chung, B.; Kim, J. et al. Ultrahigh strength, modulus, and conductivity of graphitic fibers by macromolecular coalescence. *Sci. Adv.* **2022**, *8*, eabn0939.

[30] Di, J. T.; Fang, S. L.; Moura, F. A.; Galvão, D. S.; Bykova, J.; Aliev, A.; de Andrade, M. J.; Lepró, X.; Li, N.; Haines, C. et al. Twist-stable carbon nanotube yarns and muscles by tension annealing at extreme temperatures. *Adv. Mater.* **2016**, *28*, 6598–6605.

[31] Piontkowski, Z. T.; Lipton, Z. A.; Grewal, S.; McDonald, A. E.; Trafford, M. A.; Hodges, W. L.; Chu, E. Y. S.; Pasquali, M.; Siegal, M. P.; Gilbert, S. J. et al. CNT coalescence within cnt fibers via ultraviolet pulsed laser annealing. *J. Phys. Chem. C* **2025**, *129*, 19029–19037.

[32] Yang, Z. C.; Yang, Y. N.; Huang, Y. F.; Shao, Y. Y.; Hao, H.; Yao, S. D.; Xi, Q. Q.; Guo, Y. B.; Tong, L. M.; Jian, M. Q. et al. Wet-spinning of carbon nanotube fibers: Dispersion, processing and properties. *Natl. Sci. Rev.* **2024**, *11*, nwae203.

[33] Huang, J. K.; Guo, Y. Z.; Lei, X. D.; Chen, B.; Hao, H.; Luo, J. J.; Sun, T. Z.; Jian, M. Q.; Gao, E. L.; Wu, X. Q. et al. Fabricating ultrastrong carbon nanotube fibers via a microwave welding interface. *ACS Nano* **2024**, *18*, 14377–14387.

[34] Kim, S. G.; Heo, S. J.; Kim, J. G.; Kim, S. O.; Lee, D.; Kim, M.; Kim, N. D.; Kim, D. Y.; Hwang, J. Y.; Chae, H. G. et al. Ultrastrong hybrid fibers with tunable macromolecular interfaces of graphene oxide and carbon nanotube for multifunctional applications. *Adv. Sci.* **2022**, *9*, 2203008.

[35] Ryu, K. H.; Kim, J. G.; Lee, D.; Kim, S. G.; Ku, B. C.; Hwang, J. Y.; Jeong, K. U.; Kim, N. D.; Kim, D. Y. Boost up the mechanical and electrical property of cnt fibers by governing lyotropic liquid crystalline mesophases with aramid polymers for robust lightweight wiring applications. *Adv. Fiber Mater.* **2023**, *5*, 514–526.

[36] Lee, D.; Kim, S. G.; Kim, J.; Kim, N.; Ryu, K. H.; Kim, D. Y.; Kim, N. D.; Hwang, J. Y.; Piao, Y.; An, S. M. et al. Highly conductive and mechanically strong metal-free carbon nanotube composite fibers with self-doped polyaniline. *Carbon* **2023**, *213*, 118308.

[37] Kim, S. G.; Heo, S. J.; Kim, S.; Kim, J.; Kim, S. O.; Lee, D.; Lee, S.; Kim, J.; You, N. H.; Kim, M. et al. Ultrahigh strength and modulus of polyimide-carbon nanotube based carbon and graphitic fibers with superior electrical and thermal conductivities for advanced composite applications. *Compos. Part B: Eng.* **2022**, *247*, 110342.

[38] Kim, J.; Heo, S. J.; Lee, D.; Im, B. W.; Kim, T. H.; Kim, S. G.; Ku, B. C. Highly strong carbon fibers through synergistic carbonization process of sulfonated poly(p-phenylene sulfide) and carbon nanotube. *Carbon* **2024**, *219*, 118814.

[39] Zhang, Z. Y.; Li, L. Y.; Chen, Y. Z.; Luo, J. J.; Dai, H. B.; Yang, L. X.; Qin, L. P.; Cao, J. P.; Jiao, K.; Zhang, J. From fiber to composite: *In situ* addition of graphene oxide driven structural and mechanical improvements in PBO. *Adv. Funct. Mater.* **2025**, *35*, 2501401.
[40] Qiao, X. L.; Zhu, L. T.; Gao, J.; Yang, L. Y.; Chen, W. C.; Chen, C. F.; Guan, Q. B.; You, Z. W.; Zhu, M. F. Highly robust and intrinsic flame-retardant polyphenylene benzodiazole/liquid crystal polyarylate composites for flexible triboelectric nanogenerators in harsh environment. *Adv. Mater.* **2026**, *38*, e13780.
[41] Yuan, B. L.; Yang, B.; Xu, P.; Zhang, M. Y. Poly(p-phenylene benzobisoxazole) nanofiber: A promising nanoscale building block toward extremely harsh conditions. *ACS Nano* **2025**, *19*, 1981–2012.
[42] Chen, Z. W.; Zeng, H. Y.; Girard, S. A.; Wang, F.; Chen, N.; Li, C. J. Formal direct cross-coupling of phenols with amines. *Angew. Chem., Int. Ed.* **2015**, *54*, 14487–14491.
[43] Luo, H. B.; Wang, P.; Wu, X. J.; Qu, H. R.; Ren, X. M.; Wang, Y. H. One-pot, large-scale synthesis of organic color center-tailored semiconducting carbon nanotubes. *ACS Nano* **2019**, *13*, 8417–8424.
[44] Wang, P.; Fortner, J.; Luo, H. B.; Klos, J.; Wu, X. J.; Qu, H. R.; Chen, F.; Li, Y.; Wang, Y. H. Quantum defects: What pairs with the aryl group when bonding to the sp^2 carbon lattice of single-wall carbon nanotubes. *J. Am. Chem. Soc.* **2022**, *144*, 13234–13241.
[45] Parra-Vasquez, A. N. G.; Stepanek, I.; Davis, V. A.; Moore, V. C.; Haroz, E. H.; Shaver, J.; Hauge, R. H.; Smalley, R. E.; Pasquali, M. Simple length determination of single-walled carbon nanotubes by viscosity measurements in dilute suspensions. *Macromolecules* **2007**, *40*, 4043–4047.
[46] Tsentalovich, D. E.; Ma, A. W. K.; Lee, J. A.; Behabtu, N.; Bengio, E. A.; Choi, A.; Hao, J. L.; Luo, Y. M.; Headrick, R. J.; Green, M. J. et al. Relationship of extensional viscosity and liquid crystalline transition to length distribution in carbon nanotube solutions. *Macromolecules* **2016**, *49*, 681–689.
[47] Sebastian, F. L.; Becker, F.; Yomogida, Y.; Hosokawa, Y.; Settele, S.; Lindenthal, S.; Yanagi, K.; Zaumseil, J. Unified quantification of quantum defects in small-diameter single-walled carbon nanotubes by raman spectroscopy. *ACS Nano* **2023**, *17*, 21771–21781.
[48] Gebhardt, B.; Syrgiannis, Z.; Backes, C.; Graupner, R.; Hauke, F.; Hirsch, A. Carbon nanotube sidewall functionalization with carbonyl compounds-modified Birch conditions vs the organometallic reduction approach. *J. Am. Chem. Soc.* **2011**, *133*, 7985–7995.
[49] Jeong, H. D.; Kim, S. G.; Choi, G. M.; Park, M.; Ku, B. C.; Lee, H. S. Theoretical and experimental investigation of the wet-spinning process for mechanically strong carbon nanotube fibers. *Chem. Eng. J.* **2021**, *412*, 128650.
[50] Xiao, Y.; Yang, C. J.; Zhai, X. W.; Zhao, L.; Zhao, P.; Ruan, J.; Chen, D.; Weitz, D. A.; Liu, K. Bioinspired tough and strong fibers with hierarchical core-shell structure. *Adv. Mater. Interfaces* **2023**, *10*, 2201962.
[51] Pan, H.; Zhang, Y. P.; Shao, H. L.; Hu, X. C.; Li, X. H.; Tian, F.; Wang, J. Nanoconfined crystallites toughen artificial silk. *J. Mater. Chem. B* **2014**, *2*, 1408–1414.
[52] Zhang, C.; Zhang, Y. P.; Shao, H. L.; Hu, X. C. Hybrid silk fibers dry-spun from regenerated silk fibroin/graphene oxide aqueous solutions. *ACS Appl. Mater. Interfaces* **2016**, *8*, 3349–3358.
[53] Thünemann, A. F.; Ruland, W. Microvoids in polyacrylonitrile fibers: A small-angle X-ray scattering study. *Macromolecules* **2000**, *33*, 1848–1852.
[54] Smarsly, B.; Antonietti, M.; Wolff, T. Evaluation of the small-angle X-ray scattering of carbons using parametrization methods. *J. Chem. Phys.* **2002**, *116*, 2618–2627.
[55] Miller, L. D.; Putthanarat, S.; Eby, R. K.; Adams, W. W. Investigation of the nanofibrillar morphology in silk fibers by small angle X-ray scattering and atomic force microscopy. *Int. J. Biol. Macromol.* **1999**, *24*, 159–165.
[56] Wlochowicz, A.; Janicki, J.; Slusarczyk, C. Determination of the transition region thickness in polymer blends by the SAXS method.*Compos. Interfaces* **1997**, *5*, 1–9.
[57] Jiang, X. R.; Gong, W. B.; Qu, S. X.; Wang, D. R.; Liu, T.; Li, Q. W.; Zhou, G. H.; Lu, W. B. Understanding the influence of single-walled carbon nanotube dispersion states on the microstructure and mechanical properties of wet-spun fibers. *Carbon* **2020**, *169*, 17–24.
[58] Xie, W. T.; Zhang, R. Y.; Headrick, R. J.; Taylor, L. W.; Kooi, S.; Pasquali, M.; Müftü, S.; Lee, J. H. Dynamic strengthening of carbon nanotube fibers under extreme mechanical impulses. *Nano Lett.* **2019**, *19*, 3519–3526.
[59] Luo, J. J.; Lei, X. D.; Jia, X. Z.; Li, M. D.; Yan, D.; Li, J.; Zhang, Z. Y.; Dai, H. B.; Li, C.; Zhou, W. L. et al. Aramid fibers with dynamic strength up to 10 GPa and dynamic toughness up to 700 MJ m^{-3}. *Matter* **2026**, *9*, 102496.
[60] Hyon, J.; Lawal, O.; Thevamaran, R.; Song, Y. E.; Thomas, E. L. Extreme energy dissipation via material evolution in carbon nanotube mats. *Adv. Sci.* **2021**, *8*, 2003142.
[61] Xiao, K. L.; Wu, X. Q.; Sang, Z.; Subramanian, V.; Thomas, E. L. Load sharing and accumulated bond fracture in ion-irradiated carbon mat for energy dissipation. *Sci. Adv.* **2024**, *10*, eadq3805.
[62] Cai, J. Z.; Griesbach, C.; Thevamaran, R. Extreme dynamic performance of nanofiber mats under supersonic impacts mediated by interfacial hydrogen bonds. *ACS Nano* **2021**, *15*, 19945–19955.
[63] Jung, Y.; Cho, Y. S.; Park, J. H.; Cheon, J. Y.; Lee, J. W.; Kim, J. H.; Park, C. R.; Kim, T.; Yang, S. J. Selective interbundle cross-linking for lightweight and superstrong carbon nanotube yarns. *Nano Lett.* **2023**, *23*, 3128–3136.
[64] Wan, S. J.; Li, X.; Chen, Y.; Liu, N. N.; Du, Y.; Dou, S. X.; Jiang, L.; Cheng, Q. F. High-strength scalable MXene films through bridging-induced densification. *Science* **2021**, *374*, 96–99.